Exploring the Geometry of One-Dimensional Signals

Ruiming Guo and Thierry Blu

Department of Electronic Engineering, The Chinese University of Hong Kong
1155100873@link.cuhk.edu.hk, thierry.blu@m4x.org

The wide availability of inexpensive sensors of all kinds (inertia, magnetic field, light, temperature, pressure, chemicals etc.) makes it possible to empower a host of novel applications. We have shown in a previous paper that, if the field sensed can be expressed as a finite sum of 2D sinusoids, it is possible to reconstruct the sampling curve from the 1D sequence of image samples alone (up to a linear transformation)—without extra positioning information.

Here, we explore the validity of this result if, instead, we assume the image to be directional or, as an extreme case, laminar and we simplify our previous approach to the single sinusoid fitting of segments of the 1D samples. We obtain predictive results that quantify the accuracy with which the frequencies found can be used to estimate the slope of the sampling trajectory. We also develop a robust algorithm to retrieve the sampling trajectory and estimate the laminar image that underlies the 1D samples. We finally demonstrate the validity of our approach on synthetic and well-chosen real images.

Index Terms—**Mobile sensing, frequency estimation, data visualization, sampling theory, curve estimation.**

I. Introduction

Sensor localization — With the advent of ubiquitous sensors, supporting mobility of various sensors has become an important topic in many researches. Localizing mobile sensors traversing through a physical field is a fundamental problem in this area. Accurate estimates of mobile sensor trajectories enable more efficient sensing strategies and more convenient services in various scenarios [1]. Location-dependent tasks, with application examples ranging from logistic tracking to reef monitoring or robot navigation, first and foremost require reliable positioning techniques [2].

If each mobile sensor could always equip a GPS (Global Positioning System) device, this problem would be straightforward because most of the GPS samples would usually be accurate enough to within a few meters. For applications that require positions to be monitored continuously, however, the GPS has practical limitations. First, GPS chips installed on today's mobile devices consume a substantial amount of energy, leading to a significant constraint in battery life [3], e.g. patch sensor mounted on insects (often limited to a small size). Second, in many outdoor tracking/monitoring

applications, objects often do not have a clear line-of-sight to GPS satellites [4], e.g. systems that track express delivery [5] and systems for seabed detection [6].

In order to address this issue, mobile device localization has been a subject of research studies for decades. Among the solutions investigated, triangulation methods [7], [8] are the most common. Basically, these techniques estimate mobile sensor positions based on a number of distance or angle measurements to beacon/anchor nodes. However, these methods require relatively accurate models that describe how electromagnetic signals propagate in space, and dense deployment of beacon/anchor nodes, which are unable to adapt to various real environments. Due to these limitations, people further developed trajectory mapping/matching to produce the most likely trajectory traversed by the mobile device [9], [1], [10]. In general, these methods need to pre-compute the signal-strength map or learn a signal-position mapping of the coverage area. Then, positions of the mobile device can be estimated by comparing the signal signature/fingerprints with the learned measurement map. However, the prior knowledge of the 2D physical field is usually unavailable in many situations, e.g. applications of SLAM (simultaneous localization and mapping) including planet exploration [11] and augmented reality [12].
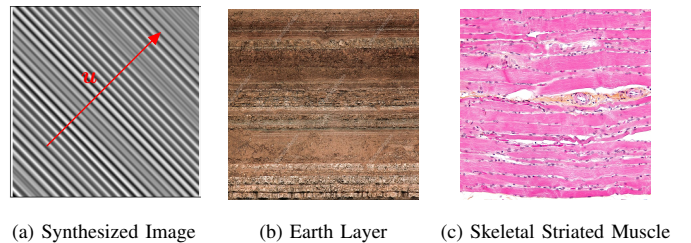

(a) Synthesized Image   (b) Earth Layer   (c) Skeletal Striated Muscle

Fig. 1: **Examples of Laminar Images.** (a) Varying fast along $\boldsymbol{u}$ (red vector) and keeping constant along $\tilde{\boldsymbol{u}}$. (b) Soil geological stratification. (c) Muscle tissue section.

Our contribution — In previous papers, we were able to demonstrate that the time samples acquired by a non-positioning sensor (e.g., temperature, pressure, magnetic, etc.) that moves within a plane, contain significant geometric information about the trajectory of the sensor [13], [14]. More precisely, if the field sensed by the sensor is approximated well by a small sum of 2D sinusoids (and if the trajectory does not change too fast) we proved that it is possible to reconstruct its trajectory (up to an affine transformation) from the 1D samples of that field along that very trajectory—and even the 2D field itsef.

Of course, what makes this result so unexpected is that *no positioning* system is used at all: it is only the spatial correlation of the field, or its manifestation through the samples along the sensor trajectory that makes this reconstruction possible. Even more surprising, the robust reconstruction algorithm that we have devised has been exceeding our expectations significantly: even when the field sensed (typically, a natural image taken with a megapixel camera) is violating the hypotheses that make our proof stand, yet a quite reasonable trajectory is retrieved (see [14, Fig. 13]). Suspecting that this possibility results from the directionality of the images considered, we replaced the sinusoidal assumption by an ideal directional assumption: the laminar image assumption (see Fig.1). The current paper reports on our findings.

Roughly speaking, the reason why we can connect 2D geometry with 1D samples is because sampling a 2D sinusoid along a straight line results in a 1D sinusoid whose frequency depends on the slope of the line. We found that, if the image is made of at least three sinusoids, the slope of the trajectory can be retrieved by finding the "projected" frequencies onto the 1D samples (up to an arbitrary affine transformation). Of course, our method relies on a very accurate high-resolution frequency estimation algorithm described originally in [15].

In contrast with that method, the current paper proposes to estimate only one sinusoid from the 1D samples: in fact, we fit the samples with a complex exponential, in practice, maximizing the discrete-time Fourier transform of the samples. This means that we do not expect the (complex-valued) sinusoidal model to fit even accurately the samples. Yet, we first observe, then demonstrate on a class of laminar images (typically, whose generator has the maximum of its frequency spectrum away from 0) that this unique frequency is a very robust predictor of the slope of the trajectory. This allows us to show that, under a constant (or varying, but known) speed hypothesis, the 2D trajectory of the sensor can be accurately retrieved up to a rotation plus a shift. We verify this finding in various conditions (real images, very noisy laminar images, etc). A decisive advantage of fitting a unique complex exponential is that this problem has an exact, non-iterative solution (relying on the roots of some polynomial), which ensures that our observations are not dependent on inaccuracies of the fitting process—as may be the case of our previous method.

This technique of extracting and visualizing 2D geometries from as little as a stream of 1D non-positioning samples could be very useful in a wide variety of practical applications. Actually, the laminar (i.e., directional) model is widespread in the real world. For instance, the earth geological formation is typically layered into separations of sediments and rocks as shown in Fig. 1 (b); muscle tissues are also layered due to their fiber structure as shown in Fig. 1 (c). A direct application is the underwater sound source localization and tracking (see Fig. 2 (a)). Due to the fast attenuation of radio waves underwater, people often choose sound waves for positioning. A very common localization technique is to identify the acoustic striation patterns of the ocean bed (at sufficient distance from the source) as shown in Fig. 2 (b) [16]. Usually, it is then necessary to deploy dense sensor arrays over a sufficiently large area so as to acquire reliable acoustic intensity images as shown in Fig. 2 (b). Taking advantage of the laminar structure of the acoustic data, our algorithm could allow to identify the distance between the mobile sensor and the source in a more economic way. As a benefit, the measured area could be enlarged significantly and the hardware cost of densely deployed sensor arrays could be largely reduced. Another direct application is geophysical imaging that aims to map the geological structure and formation of the subsurface, a core procedure in many geo-industrial applications, e.g. oil/gas prospecting and ocean bottom sensing as shown in Fig. 2 (c). By reinterpreting the retrieved 2D geometry (e.g. image directionality, slopes, etc.) geologically, our method could possibly be incorporated into the existing seismic imaging techniques to provide clearer and cleaner subsurface images.

(a) Sound source localization   (b) Sound striation patterns   (c) Stratum imaging
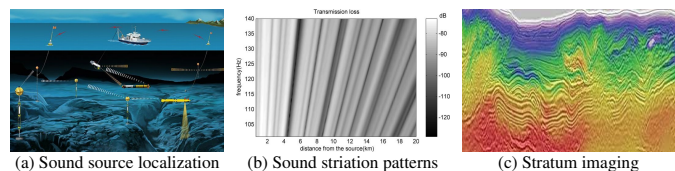
Fig. 2: A variety of potential applications. (a) Hydroacoustic positioning. (b) acoustic striation patterns. (c) Seismic imaging in oil/gas detection.

Finally, we would like to point out that our method is more than trajectory retrieval, as it also provides a new visualization tool to interpret arbitrary (non-geometric) 1D time-series geometrically. By checking the sample-mismatch level (see Section IV), we can quantitatively measure the "laminarity" of the underlying (fictitious) image, using only the available 1D data. In particular, our method may prove useful to visualize a host of real 1D signals without explicit 2D origin, such as speech, music, biomedical signals etc. We believe that the retrieved 2D geometric features (such as trajectory curvature, crossings, length etc.) could be used for discrimination, classification and recognition.

Structure of the paper — Section II describes the methodology of trajectory retrieval using the unique-sinusoid fitting strategy: we first provide a visual intuition of how the frequencies found relate to the slope of a linear trajectory, and give examples ranging from synthetic laminar images to real images, that demonstrate the determinism and consistency of these frequencies; then we provide a mathematical explanation to validate the visual observation, which gives rise to the laminar sampling theorem. We develop the reconstruction hypotheses and detail the complete method that leads to an efficient algorithm in Section III. Experimental results including simulations on synthetic laminar images, and tests on real images are presented in Section IV. We conclude the paper by summarizing our main results and evoking possible extensions of this work (Section V).

II. THE GEOMETRY IN THE SAMPLES OF A LAMINAR IMAGE

A. Sampling a Laminar Image Along a Curve

We are given a sequence of 1D (non-positioning) sensor measurements $s_n = I(\mathbf{r}(n/F_s))$ sampled uniformly (sampling frequency $= F_s$) from a 2D laminar image defined by

$$I(\mathbf{r}) = g(\mathbf{u}^\mathsf{T} \mathbf{r}), \qquad \text{where } \|\mathbf{u}\| = 1 \tag{1}$$

along some *unknown 2D trajectory* $\mathbf{r}(t)$. The goal is then to retrieve that trajectory. Fig. 3 provides a visual depiction of this problem.

At first glance, this objective seems unreasonable because the problem is seriously ill-posed due to the loss of bidimensional information. However, we know from [14], [17] that the geometry of the trajectory can be retrieved from these samples when the image is made of a sum of 2D sinusoids. We will show that, by just fitting the samples with a single 1D sinusoid, we can readily retrieve valuable geometric features as well, when the image is laminar. Moreover, we will demonstrate that these features are quite consistent along the trajectory, and very robust in noisy/model mismatch conditions. Our purpose is to utilize them to achieve trajectory retrieval (up to a rotation plus a shift).

(a): Laminar image (b): Sampling trajectory
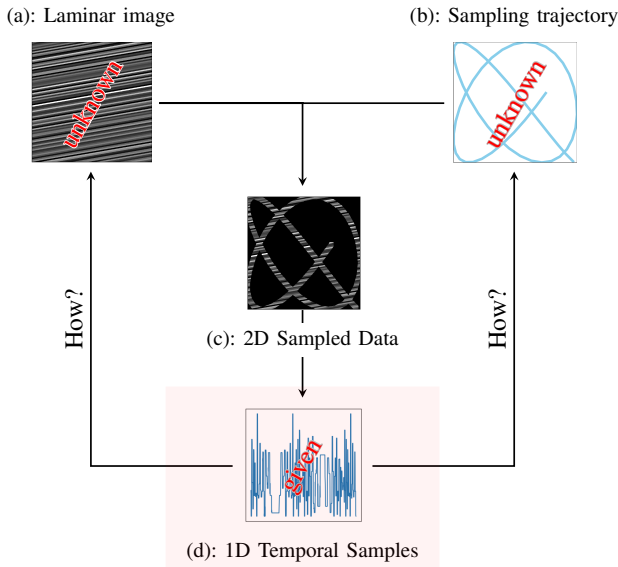
(c): 2D Sampled Data

(d): 1D Temporal Samples

Fig. 3: Our goal is to retrieve the sampling trajectory (b) of the mobile sensor and the image (a) from the measured 1D samples (d) (framed in red box).

B. Visual Intuition

First, we observe that sampling a laminar image along straight lines of different orientations results in roughly scaled versions of the same 1D signal (see Fig. 4 (a)). This observation still holds for real images with clear directionality as shown in Figs. 4 (b) and (c).

We propose to identify this scale change by computing the frequency ω of the complex exponential that best fits the samples of the image $I(\mathbf{r})$ along a straight line parametrized
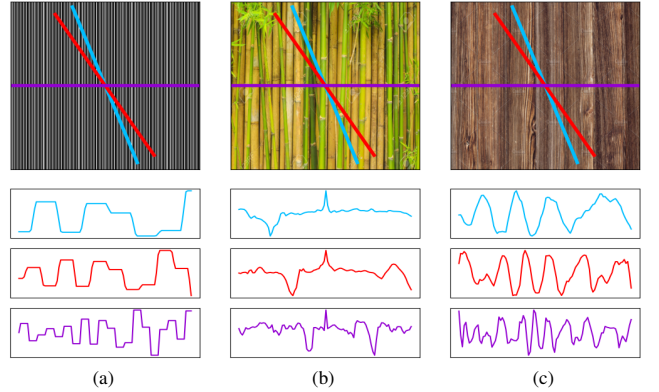

Fig. 4: **Scaling feature of the 1D laminar samples.** (a) From top to bottom: sampling the synthetic laminar along different directions gives rise to a precise scaling relationship. Moreover, this scaling relationship still holds approximately for many natural images, like (b) and (c).

as $\mathbf{r}(t) = \mathbf{a}t + \mathbf{b}$. Ideally, we want to find $\hat{\omega}$ that minimizes the power spectrum density-like criterion

$$J(\omega) = \inf_{A \in \mathbb{C}} \lim_{T \to \infty} \frac{1}{T} \int_{-T/2}^{T/2} |I(\mathbf{r}(t)) - A e^{j\omega t}|^2 \, \mathrm{d}t. \tag{2}$$

In practice, though, we will minimize a windowed version of (2)

$$J(\omega) = \inf_{A \in \mathbb{C}} \int w_T(t) |I(\mathbf{r}(t)) - A e^{j\omega t}|^2 \, \mathrm{d}t, \tag{3}$$

where $w_T(t)$ is a positive function of integral one, that we will typically choose to be Gaussian

$$w_T(t) = \frac{1}{\sqrt{4\pi T^2}} \exp\left(-\frac{t^2}{4T^2}\right). \tag{4}$$

In practice, we work with discrete samples, that we assume to be obtained at a frequency F_s that is large enough for the integrals involved in (2) and (3) to be well approximated by Riemann summations.

As is well-known, this type of optimization amounts to maximizing the absolute value of the windowed Fourier transform of the samples. Note that both $\hat{\omega}$ and $-\hat{\omega}$ are solutions of the minimization of (2) and (3) because the 1D samples are real-valued. We give an algorithm in the supplementary materials, that finds the solutions of the minimization of a discretization of (3) exactly.

Of course, we do not pretend that the samples $I(\mathbf{r}(t))$ can be accurately fitted by a complex exponential. Yet, we will show that the frequency obtained as a result of this minimization changes linearly with the scale change; i.e., with $\mathbf{u}^\mathsf{T} \mathbf{a}$ since $I(\mathbf{r}(t)) = g(\mathbf{u}^\mathsf{T} \mathbf{a}t + \mathbf{u}^\mathsf{T} \mathbf{b})$. This means that, eventually, the orientation of the line, $\mathbf{a}$, can be retrieved from this scale change.

Rotational continuity — We design a rotation experiment to further visualize the relation between the angle of the line and the frequency retrieved: for every angle of the straight line segment, we compute the optimal frequency (2) and plot the relation between these two variables (see Fig. 5). The estimated 1D frequencies show a very consistent pattern, as

can be checked by following their visual continuity.

Interestingly, we observe that the frequency pattern obtained is also very robust to noise. We add strong white noise (PSNR = 0 dB, see Fig. 6(a)) to the laminar image in Fig. 5(a): the comparison of the frequency patterns in Fig. 6(b) vs Fig. 5(b) for the two images shows that they are very similar.

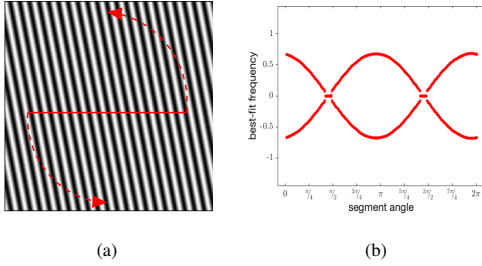Moreover, we observe that continuous frequency patterns

Fig. 5: **Rotation test.** (a) Laminar image. (b) Graph showing the frequency of the sinusoid that best fits the samples along a straight line ("segment") with varying orientation angles. Notice that two symmetric solutions $\hat{\omega}$ and $-\hat{\omega}$ are the optimal solutions to the fitting problem 2 (real-valued samples).
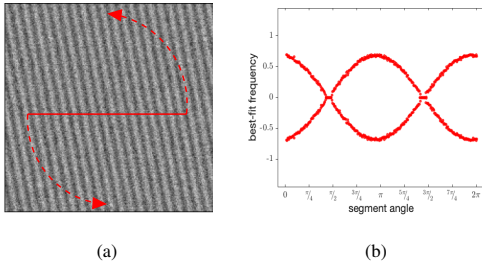

Fig. 6: **Robustness of the designed rotation pattern against noise.** (a) Noisy Laminar image (PSNR = 0 dB). (b) Rotation pattern of the signal scaling feature. Observe that, the rotation pattern is very robust to noise.
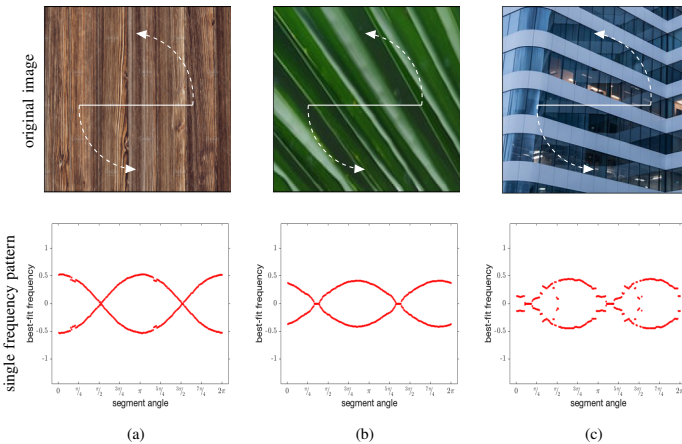

Fig. 7: **Examples of success.** From top to bottom: test images; estimated 1D scaling features; denoised 1D scaling features. From left to right: (a) Wood grain; (b) Needle Leaves; (c) Building. We can observe that there are deterministic patterns in the raw 1D scaling features (second row).

are surprisingly widespread in many "less-laminar" real images. The continuity of the patterns are made even more obvious if we include the "second best" frequency obtained in the minimization of (3) (see Fig. 7 and also Fig. 2 of the supplementary materials).

These visual observations suggest that the "best fitting" frequency of the samples of an image along a straight line is related to the slope of this line. Eventually, this indicates that, by estimating the local frequency of 1D samples, it is possible to reconstruct the 2D trajectory along which the ("laminar-like") image has been sampled. However, frequency continuity is not sufficient for that purpose. It is also necessary for the angle-to-frequency pattern to reflect directly the scale change that results from an orientation change; i.e., that frequency $\propto \sin(\text{angle} + \text{const})$ — Rotational continuity, see Section II-C for details.

On the other hand, images that are less directional are less likely to exhibit the rotational continuity that characterizes "laminar-like" images or even mere continuity of the frequency pattern (see Fig. 2 in the supplementary materials).

C. Theory

How can the consistency of the patterns observed in the previous subsection be explained mathematically? We first explore the theory under the ideal situation where the observation window is of infinite length, and then extend it to the practical case of windows of finite length.

Infinite window — Let us denote $s(t) = I\big(\mathbf{r}(t)\big)$ and assume that the limits

$$P_s = \lim_{T \to \infty} \frac{1}{T} \int_{-T/2}^{T/2} \big|s(t)\big|^2 \, \mathrm{d}t,$$

$$A_s(\omega) = \lim_{T \to \infty} \frac{1}{T} \int_{-T/2}^{T/2} s(t) e^{-j\omega t} \mathrm{d}t$$

are well-defined: this is in particular the case when $s(t)$ is a finite sum of complex exponentials. A useful result is that, when $s(t) = c e^{j\omega_0 t}$ then $P_s = |c|^2$ and

$$A_s(\omega) = c \, \mathbb{1}(\omega - \omega_0) = \begin{cases} c, & \text{if } \omega = \omega_0; \\ 0, & \text{otherwise.} \end{cases} \quad (5)$$

which is readily obtained by replacing $s(t) = c e^{j\omega_0 t}$ in the expression that defines $A_s(\omega)$.

Theorem 1. *Assume that the image $I(\mathbf{r})$ is made of a finite sum of complex exponentials*

$$I(\mathbf{r}) = \sum_{k=1}^{K} c_k \exp(j\boldsymbol{\omega}_k^\mathsf{T}\mathbf{r})$$

where K is finite, c_k are complex-valued coefficients and $\boldsymbol{\omega}_k$ are real-valued 2D vectors. Denote by $s(t)$ the samples of this image along the straight line defined by $\mathbf{r}(t) = t\mathbf{a} + \mathbf{b}$, where we assume that all the $\boldsymbol{\omega}_k^\mathsf{T}\mathbf{a}$ are distinct. Then the minimum of (2) over all ω is attained by $\boldsymbol{\omega}_{k_0}^\mathsf{T}\mathbf{a}$ where the index k_0 is such that $|c_{k_0}| = \max_k |c_k|$ (several solutions possible).

Proof. Minimizing the ideal criterion (2) is equivalent to maximizing $|A_s(\omega)|^2$ over all values of ω because

$$\lim_{T\to\infty}\frac{1}{T}\int_{-T/2}^{T/2}\big|s(t)-Ae^{j\omega t}\big|^2\,\mathrm{d}t$$
$$=S^2-2\mathrm{Re}\big\{A^*A_s(\omega)\big\}+|A|^2$$
$$\geq S^2-|A_s(\omega)|^2$$

for all $A\in\mathbb{C}$, with equality if and only if $A=A_s(\omega)$.

Now, when

$$s(t)=I(\mathbf{r})=\sum_{k=1}^{K}c_k\exp(j\boldsymbol{\omega}_k^\mathsf{T}\mathbf{b})\exp(jt\boldsymbol{\omega}_k^\mathsf{T}\mathbf{a})$$

$A_s(\omega)$ can be expressed as

$$A_s(\omega)=\sum_{k=1}^{K}\lim_{T\to\infty}\frac{c_k\exp(j\boldsymbol{\omega}_k^\mathsf{T}\mathbf{b})}{T}\int_{-T/2}^{T/2}\exp\big(jt(\boldsymbol{\omega}_k^\mathsf{T}\mathbf{a}-\omega)\big)\mathrm{d}t,$$
$$=\sum_{k=1}^{K}c_k\exp(j\boldsymbol{\omega}_k^\mathsf{T}\mathbf{b})\mathbb{1}(\omega-\boldsymbol{\omega}_k^\mathsf{T}\mathbf{a}).$$

Since, by assumption, all the $\boldsymbol{\omega}_k^\mathsf{T}\mathbf{a}$ are distinct, the above expression is non-zero only when $\omega=\boldsymbol{\omega}_k^\mathsf{T}\mathbf{a}$ and, in that case, $|A_s(\omega)|=|c_k|$. Hence, the maximum of $|A_s(\omega)|$ is attained when the amplitude $|c_k|$ is maximal. $\square$

It is important to stress that the minimization of (2) results in the maximization of a function, $|A_s(\omega)|$, whose local maxima arise exactly at the frequencies $\boldsymbol{\omega}_k^\mathsf{T}\mathbf{a}$. This shows that, not only the global maximum, but also the local maxima follow the same pattern: the scalar product between an image dependent feature (2D frequency), and the slope of the sampling line.

Corollary 1. *Assume that the image $I(\mathbf{r})$ is laminar; i.e., $I(\mathbf{r})=g(\mathbf{u}^\mathsf{T}\mathbf{r})$ where the g is a univariate "generator", for which we assume that $|A_g(\omega)|$ has a unique maximum at $\omega=\omega_g$, the generator frequency. Denote by $s(t)$ the samples of this image along the straight line defined by $\mathbf{r}(t)=t\mathbf{a}+\mathbf{b}$, then the minimum of (2) over all ω is attained by $\omega=\omega_g\,\mathbf{u}^\mathsf{T}\mathbf{a}$.*

Proof. Using that $s(t)=g(t\mathbf{u}^\mathsf{T}\mathbf{a}+\mathbf{u}^\mathsf{T}\mathbf{b})$, we find

$$A_s(\omega)=\lim_{T\to\infty}\frac{1}{T}\int_{-T/2}^{T/2}g(t\mathbf{u}^\mathsf{T}\mathbf{a}+\mathbf{u}^\mathsf{T}\mathbf{b})e^{-j\omega t}\mathrm{d}t$$
$$=\lim_{T\to\infty}\frac{e^{j\omega\mathbf{u}^\mathsf{T}\mathbf{b}/\mathbf{u}^\mathsf{T}\mathbf{a}}}{T|\mathbf{u}^\mathsf{T}\mathbf{a}|}\int_{-T|\mathbf{u}^\mathsf{T}\mathbf{a}|/2+\mathbf{u}^\mathsf{T}\mathbf{b}}^{T|\mathbf{u}^\mathsf{T}\mathbf{a}|/2+\mathbf{u}^\mathsf{T}\mathbf{b}}g(t)e^{-j\omega t/\mathbf{u}^\mathsf{T}\mathbf{a}}\mathrm{d}t$$
$$=e^{j\omega\mathbf{u}^\mathsf{T}\mathbf{b}/\mathbf{u}^\mathsf{T}\mathbf{a}}A_g(\omega/\mathbf{u}^\mathsf{T}\mathbf{a}).$$

Hence, the maximum of $|A_s(\omega)|$ is attained by $\omega=\pm\omega_g\,\mathbf{u}^\mathsf{T}\mathbf{a}$, where $\pm\omega_g$ is the frequency for which $|A_g(\omega)|$ is maximum. $\square$

This demonstrates that, if the generator frequency is different from 0, then the frequency obtained through the minimization of the ideal criterion (2) provides one component, $\mathbf{u}^\mathsf{T}\mathbf{a}$, of the slope $\mathbf{a}$ of the sampling line, up to a multiplicative constant, which is what was observed in Figs 5, 6 and real image examples (also see Fig. 1 in the supplementary materials).

Cor. 1 is actually more useful than Thm. 1 when K is large because, in that case, the condition on the distinctness of the frequencies along the slope $\mathbf{a}$ is prohibitive: if the 2D frequencies $\boldsymbol{\omega}_k$ are not pairwise parallel, there are $\binom{K}{2}=K(K-1)/2$ possible values of $\mathbf{a}$ that make $\boldsymbol{\omega}_k^\mathsf{T}\mathbf{a}=\boldsymbol{\omega}_{k'}^\mathsf{T}\mathbf{a}$ for some k,k'. Obviously, this would result in too many "forbidden" slope directions for the statement of Thm. 1 to be useful.

Instead, when all the frequencies are parallel (laminar image), the condition reduces to avoiding that $\mathbf{a}$ and $\boldsymbol{\omega}_k$ are perpendicular, in which case the optimal frequency retrieved is zero. For all the other frequencies, the conversion to a slope orientation is feasible.

Finite window — In practice, we have only a finite number of samples and we have to optimize the criterion (3) instead. In order to be able to use the optimization results of Thm 1 and Cor 1, we have to show that the frequency obtained is not "too different" from the ideal one—which provides the orientation of the sampling line.

Notation. *Assume that the image $I(\mathbf{r})$ is the real part of a sum of complex exponentials*

$$I(\mathbf{r})=\mathrm{Re}\big\{c_0\exp(j\boldsymbol{\omega}_0^\mathsf{T}\mathbf{r})\big\}+\sum_{k=1}^{+\infty}c_k\exp(j\boldsymbol{\omega}_k^\mathsf{T}\mathbf{r})\qquad(6)$$

where c_k are complex-valued coefficients ($|c_0|>|c_k|,k\geq1$) and $\boldsymbol{\omega}_k$ are real-valued 2D vectors. Then, for $\boldsymbol{\omega}_0^\mathsf{T}\mathbf{a}\neq0$, we denote

$$\begin{cases}\gamma_0=1-\sup_{k\geq1}\dfrac{|c_k|}{|c_0|}\geq0\\[2mm]\Delta_0=\inf_{k\geq1}\Big(\Big|\dfrac{\boldsymbol{\omega}_k^\mathsf{T}\mathbf{a}}{\boldsymbol{\omega}_0^\mathsf{T}\mathbf{a}}-1\Big|,\Big|\dfrac{\boldsymbol{\omega}_k^\mathsf{T}\mathbf{a}}{\boldsymbol{\omega}_0^\mathsf{T}\mathbf{a}}+1\Big|\Big)\\[2mm]\Delta_1=\inf_{k\neq k'\geq1}\dfrac{|(\boldsymbol{\omega}_k-\boldsymbol{\omega}_{k'})^\mathsf{T}\mathbf{a}|}{|\boldsymbol{\omega}_0^\mathsf{T}\mathbf{a}|}\end{cases}$$

which allows us to define the positive function (which may assume infinite values)

$$Q(\lambda)=(1-\gamma_0)\left(1+\frac{e^{-\lambda^2\Delta_1^2/4}}{1-e^{-3\lambda^2\Delta_1^2/4}}+\frac{2e^{-\lambda^2\Delta_0^2}}{1-e^{-3\lambda^2\Delta_0^2}}\right)+2e^{-\lambda^2}.$$

Theorem 2. *Denote by $s(t)$ the samples of the image (6) along the straight line $\mathbf{r}(t)=t\mathbf{a}+\mathbf{b}$. Then, if $Q(T\boldsymbol{\omega}_0^\mathsf{T}\mathbf{a})<1$, the minimization of (3) over $\omega\in\mathbb{R}$ results in a frequency $\hat{\omega}$ which is such that*

$$\big||\boldsymbol{\omega}_0^\mathsf{T}\mathbf{a}|-|\hat{\omega}|\big|\leq\frac{\sqrt{-\log(1-Q(T\boldsymbol{\omega}_0^\mathsf{T}\mathbf{a}))}}{T}.$$

Please see Appendix C for the proof. When T is sufficiently large, this uncertainty reduces to $\sqrt{-\log\gamma_0}/T$. This uncertainty is small when, either γ_0 is closer to 1 (i.e., the laminar image is essentially made of a single sinusoid), or when T is large, which can compensate for small values of γ_0 (i.e., when the laminar image has a richer frequency contents). Also note that the condition $Q(T\boldsymbol{\omega}_0^\mathsf{T}\mathbf{a})<1$ automatically rules out the possibility that $\gamma_0=0$—in which case $Q(\lambda)>1$ for all $\lambda\geq0$.

Applying this theorem to a laminar image (1), we have the following results on the sinusoid fitting accuracy (see Appendix D for the proof):

Corollary 2. *Assume the 2D image frequencies are all along the direction $\mathbf{u}$, i.e.*

$$\boldsymbol{\omega}_0 = \omega_g \mathbf{u}, \boldsymbol{\omega}_k = \omega_k \mathbf{u}, k \geq 1.$$

We denote by $\hat{\lambda}$ the unique value of λ for which $Q(\lambda) = 1$. Then, if $|\mathbf{u}^\mathsf{T}\mathbf{a}| > \hat{\lambda}/(\omega_g T)$, minimizing (3) over $\omega \in \mathbb{R}$ results in a frequency $\hat{\omega}$ that provides the geometric information $|\mathbf{u}^\mathsf{T}\mathbf{a}|$ up to an uncertainty

$$\left| |\mathbf{u}^\mathsf{T}\mathbf{a}| - |\hat{\omega}/\omega_g| \right| \leq \frac{\sqrt{-\log(1 - Q(\omega_g T \mathbf{u}^\mathsf{T}\mathbf{a}))}}{\omega_g T}. \quad (7)$$

When $|\mathbf{u}^\mathsf{T}\mathbf{a}|$ is not very close to $\hat{\lambda}/(\omega_g T)$, this uncertainty reduces to $\sqrt{-\log \gamma_0}/(\omega_g T)$.

Although an exact expression of $\hat{\lambda}$ mixes in an intricate way Δ_0, Δ_1 and γ_0, a close lower bound is given by:

$$\hat{\lambda} > \max\left(\sqrt{-\log \gamma_0}, \frac{2\sqrt{-\log \gamma_1}}{\Delta_1}, \frac{\sqrt{-\log \gamma_2}}{\Delta_0} \right)$$

where

$$\gamma_1 = \sqrt[3]{\frac{1}{2} + \sqrt{\frac{1}{4} + \frac{(1-\gamma_0)^3}{27\gamma_0^3}}} + \sqrt[3]{\frac{1}{2} - \sqrt{\frac{1}{4} + \frac{(1-\gamma_0)^3}{27\gamma_0^3}}},$$

$$\gamma_2 = \sqrt[3]{\frac{1}{2} + \sqrt{\frac{1}{4} + \frac{8(1-\gamma_0)^3}{27\gamma_0^3}}} + \sqrt[3]{\frac{1}{2} - \sqrt{\frac{1}{4} + \frac{8(1-\gamma_0)^3}{27\gamma_0^3}}}.$$

It should be noted that, our requirement $|\mathbf{u}^\mathsf{T}\mathbf{a}| > \hat{\lambda}/(\omega_g T)$ automatically ensures that the generator frequency is different from 0. Several useful observations can be deduced from Corollary 2, for the frequency estimation technique to yield reliable geometric information:

- first, since $Q(\lambda) > 1 - \gamma_0$, the sampling line segment should be long enough so that the uncertainty $\sqrt{-\log \gamma_0}/(\omega_g T)$ is controlled (see Section III-B): T can be short if the laminar image is essentially made of one sinusoid, but in more complex cases (sinusoids of close amplitudes), it has to be larger;
- second, even when the segment is long enough, line directions that are too close to the laminar direction (perpendicular to $\mathbf{u}$) cannot be retrieved accurately: given the lower bounds on $\hat{\lambda}$, the scalar product $|\mathbf{u}^\mathsf{T}\mathbf{a}|$ has to be larger than $\sqrt{-\log \gamma_0}/(\omega_g T)$, and this lower bound deteriorates when the image changes too slowly. Similarly, assuming that $\Delta_1 \approx \Delta_0$, the scalar product $|\mathbf{u}^\mathsf{T}\mathbf{a}|$ has also to be larger than $2\sqrt{-\log \gamma_2}/(\Delta_1 \omega_g T)$, which shows that the direction estimation deteriorates when the frequencies of the laminar image are too close to each other—irrespective of their amplitudes.

Corollary 2 is able to explain the pattern seen in Fig. 5: assuming that $\mathbf{a} = \left(\cos\theta, \sin\theta\right)^\mathsf{T}$ ($\|\mathbf{a}\| = 1$ for simplicity here) where θ is the "segment angle", Corollary 2 predicts that, when $|\mathbf{u}^\mathsf{T}\mathbf{a}| > \hat{\lambda}/(\omega_g T)$—i.e., when θ is away from the intervals $\pi/2 + n\pi + [-\arccos(\hat{\lambda}/(\omega_g T)), \arccos(\hat{\lambda}/(\omega_g T))]$ (n integer)—the graph of the optimal frequency in function of θ is essentially the graph of $\omega_g \mathbf{u}^\mathsf{T}\mathbf{a} = \omega_g \cos\theta$; wheras, when θ is in the intervals $\pi/2 + n\pi +$
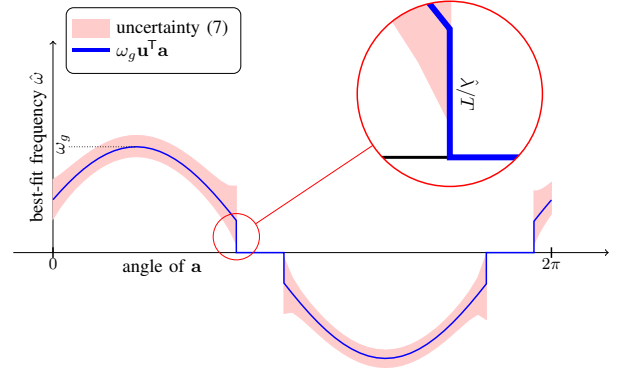

Fig. 8: Visualization of the results of Corollary 2, in relation to the rotation experiments of Section II-B.

$[-\arccos(\hat{\lambda}/(\omega_g T)), \arccos(\hat{\lambda}/(\omega_g T))]$ (n integer), the error is not controlled and, in practice, the optimization algorithm returns 0 as the best-fit frequency (see Fig. 8).

Clearly, $\hat{\lambda}$ is a critical value which characterizes the "conditioning" of a laminar image, independently of the segment length T and of the main laminar frequency ω_g. In practice, given a laminar image, ω_g and $\hat{\lambda}$ can be figured out directly from a rotation experiment: choosing a value of T for which the sinusoidal pattern is readily observed, ω_g is obtained from the maximum amplitude of that sinusoid, whereas $\hat{\lambda}$ is obtained from the discontinuity jump (see zoomed area in Fig. 8) that characterizes the loss of accuracy of the frequency estimation when the laminar image is sampled along the laminar direction.

III. RECONSTRUCTION OF SAMPLING TRAJECTORIES

We have seen (Sections II-B and II-C) that estimating a single frequency from the samples of a laminar image provides the slope of the sampling line, up to a multiplicative constant, ω_g, defined in Cor. 1. In order to generalize this result to arbitrary curves, we need to be able to approximate them accurately by piecewise-linear segments of fixed length T, and to calculate this constant. To this end, we essentially need the trajectory of the sensor to have a small curvature, and that one of its slopes, at least, corresponds to the largest frequency achieved when considering all orientation angles.

A. Hypotheses

In details, however, we need more specific hypotheses on the kinematics of sensor:

1) Velocity-related:
   a) the speed of the sensor $\|\mathbf{r}'(t)\|$ is a constant, which we practically set to 1 in the rest of the paper;
   b) there exist sampling points where the trajectory is *perpendicular* to the laminar direction; and these points are *not inflection points* (visualization: see Fig. 5a and 5b in the supplementary materials).
2) Acceleration-related: continuous differentiability of the curvature at most points on the trajectory or, more accurately, quadratic predictibility of the first order derivative

$\mathbf{r}'(t)$, which provides a rule to choose between several frequency estimates;

In addition, we also need prior knowledge of $\kappa_{\max}$ (i.e. the maximum curvature of the trajectory) and of $\hat{\lambda}$ for which $Q(\hat{\lambda}) = 1$.

B. Parameter determination

Trajectory retrieval relies on specifying a segment length, T, and on identifying the proportionality constant ω_g involved in Corollary 2.

Estimation of the generator frequency — The generator frequency ω_g can be estimated by exploiting Hypothesis 1b which states that there exists a point on the trajectory where the mobile sensor moves *perpendicular* to the laminar direction— hence, parallel to $\mathbf{u}$. As a consequence, this constant can be obtained according to

$$\omega_g = \max_t \frac{|\omega(t)|}{\|\mathbf{r}'(t)\|} = \max_t |\omega(t)| \tag{8}$$

since $\|\mathbf{r}'(t)\| = 1$ according to Hypothesis 1a.

Determination of the segment length — Considering the curvature of the trajectory: in a $[t_0 - T/2, t_0 + T/2]$ neighborhood, the parabolic approximation (second-order Taylor) of the curve parametrization takes the form

$$\mathbf{r}(t) = \mathbf{r}(t_0) + (t - t_0)\mathbf{r}'(t_0) + \frac{\kappa(t_0)(t - t_0)^2}{2}\tilde{\mathbf{r}}'(t_0) \tag{9}$$

where $\tilde{\mathbf{r}}'(t_0)$ is the unit vector perpendicular (counterclockwise) to $\mathbf{r}'(t_0)$, and $\kappa(t_0)$ is the curvature at t_0 (from Frenet-Serret's formulas). Hence, $\kappa_{\max} = \max_{t_0} |\kappa(t_0)|$ (of which we have prior knowledge) should be small, to ensure the closeness between the curve and its closest piecewise-linear approximation, yet not too small, to prevent the curve direction from staying parallel to the laminar direction over more than one segment. More precisely:

- given that the best approximation of (9) by a straight line $\mathbf{r}(t) = (t - t_0)\mathbf{a} + \mathbf{b}$ leads to $\mathbf{a} = \mathbf{r}'(t_0)$ and a minimal error of $|\kappa(t_0)|T^2/16$, we typically require that this error is smaller than 3% of the segment length; i.e., $\kappa_{\max}T \leq 1/2$;
- from Corollary 2, in order to guarantee that $|\mathbf{u}^\mathsf{T}\mathbf{r}'(t_0)|$ and $|\mathbf{u}^\mathsf{T}\mathbf{r}'(t_0 \pm T)|$ are not altogether $\leq \hat{\lambda}/(\omega_g T)$, we need that $|\mathbf{u}^\mathsf{T}\mathbf{r}'(t_0 \pm T) - \mathbf{u}^\mathsf{T}\mathbf{r}'(t_0)| \geq \hat{\lambda}/(\omega_g T)$ when $\mathbf{u}^\mathsf{T}\mathbf{r}'(t_0)$ is close to zero; i.e., $|\kappa(t_0 \pm T/2)| \geq \hat{\lambda}/(\omega_g T^2)$, which implies that $\kappa_{\max} \geq \hat{\lambda}/(\omega_g T^2)$.

As a consequence, the segment length T is constrained by

$$\sqrt{\frac{\hat{\lambda}}{\omega_g \kappa_{\max}}} \leq T \leq \frac{1}{2\kappa_{\max}}. \tag{10}$$

In principle, any value of T within this "safe" range is acceptable for our method.

C. Frequency tracking

We find the minimum of (3) for every segment of samples acquired by the sensor, which provides a sequence of frequencies, indexed by the segment index. However, there are two issues to consider:

1) both ω and $-\omega$ are the optimal solutions of the minimization of (3), since the sensor samples are real-valued;
2) the fitting frequency is less reliable when its absolute value is small; i.e., when the sampling curve is parallel to the laminar direction—perpendicular to $\mathbf{u}$.

Hence, finding the frequency of each segment amounts to selecting correctly either $+\omega$ or $-\omega$.

The key idea that makes it possible to track the fitting frequency of each segment is based on the continuity of the trajectory slopes (Hypothesis 2). As a result, the scalar product $\mathbf{u}^\mathsf{T}\mathbf{r}'(t)$ is continuous which guarantees that, as long as the values found are significantly different from zero, we can unambiguously identify which of $\pm\omega$ is the correct result.

When the values found get closer to zero, we have to use a more quantitative prediction principle. Thanks to Hypothesis 2, we know that the first order derivative $\mathbf{r}'(t)$ can be approximated locally by a quadratic function of t. In other words, the frequency of a trajectory segment can be predicted by fitting a quadratic model to its adjacent frequencies (typically six). The decision between $+\omega$ and $-\omega$ can then be made by choosing the sign that results in the smallest prediction error. A further refinement of this strategy consists in testing the quadratic prediction with the "second best" fitting frequencies as well, then choosing the best one of the four frequency candidates.

A causal (towards increasing values of t) implementation of our frequency tracking approach requires initialization, which can be performed by trying all choice options (i.e., four different frequencies) for all the samples used at once in the prediction formula (typically six samples), and retaining the choice that minimizes the prediction error.

D. Slope and trajectory

Once the proportionality constant ω_g is known, the scalar product $\mathbf{u}^\mathsf{T}\mathbf{r}'(t_0)$ of the trajectory segment centered at $t = t_0$ can be retrieved from the frequencies that are tracked in each curve segment according to the formula $\mathbf{u}^\mathsf{T}\mathbf{r}'(t) = \omega(t)/\omega_g$. From such scalar products, the complete slope of the trajectory can be calculated at every point since $\|\mathbf{u}\| = 1$, although it will be necessary to remove a sign ambiguity in this process. Finally, integrating the slope provides the trajectory of the sensor.

More precisely, denoting by $\tilde{\mathbf{u}}$ the unit vector perpendicular to $\mathbf{u}$ in the counterclockwise orientation (i.e., $\det(\mathbf{u}, \tilde{\mathbf{u}}) = 1$), from $\mathbf{u}^\mathsf{T}\mathbf{r}'(t)$ we get $\tilde{\mathbf{u}}^\mathsf{T}\mathbf{r}'(t) = \pm\sqrt{\|\mathbf{r}'(t)\|^2 - (\mathbf{u}^\mathsf{T}\mathbf{r}'(t))^2}$, where $\|\mathbf{r}'(t)\|$ is a known constant. How can the sign of this expression be determined without ambiguity? For this, we apply two principles:

1) predictability of the slope (Hypothesis 2), which guarantees that, for values of t where the adjacent values of $\mathbf{u}^\mathsf{T}\mathbf{r}'(t)$ are not close to the maximum, $\|\mathbf{r}'(t)\|$, then the calculated $\tilde{\mathbf{u}}^\mathsf{T}\mathbf{r}'(t)$ should have the same sign;
2) no inflection points have a slope parallel to $\mathbf{u}$ (Hypothesis 1b) which guarantees that when $\mathbf{u}^\mathsf{T}\mathbf{r}'(t)$ reaches its maximum, then the signum of $\tilde{\mathbf{u}}^\mathsf{T}\mathbf{r}'(t)$ changes as it crosses 0.

Once $\mathbf{u}^\mathsf{T}\mathbf{r}'(t)$ and $\tilde{\mathbf{u}}^\mathsf{T}\mathbf{r}'(t)$ have been calculated, we obtain $\mathbf{r}'(t)$ as

$$\mathbf{r}'(t) = \mathbf{u}^\mathsf{T}\mathbf{r}'(t) \cdot \mathbf{u} + \tilde{\mathbf{u}}^\mathsf{T}\mathbf{r}'(t) \cdot \tilde{\mathbf{u}}, \qquad (11)$$

which can then be integrated to yield $\mathbf{r}(t)$, up to a shift. Of course, since $\mathbf{u}$ is unknown, this also means that the trajectory is retrieved up to an arbitrary rotation.
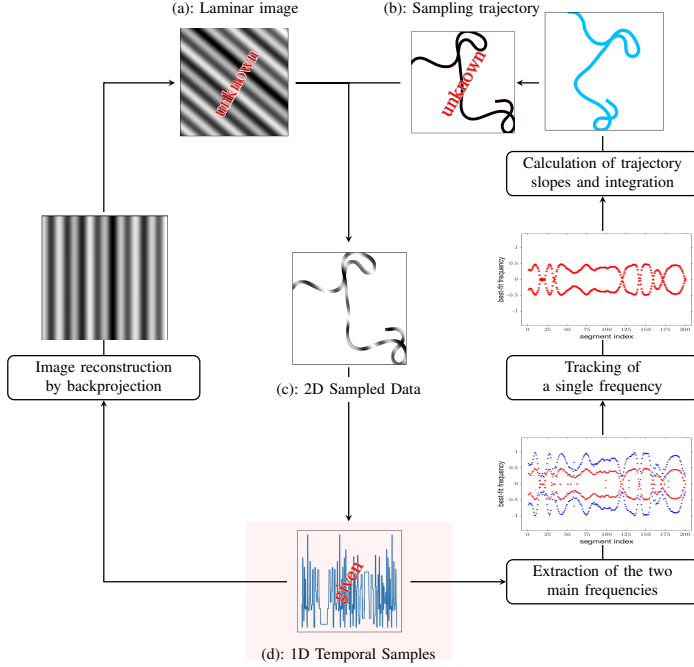

Fig. 9: Flowchart of the retrieval algorithm: the 2D trajectory (b) can be accurately reconstructed (up to a rotation plus a shift) from the 1D samples (d), whereas the image is retrieved by "backprojecting" the samples along the laminar direction.

E. Image reconstruction

Together with the sampling trajectory $\mathbf{r}(t)$, the 2D laminar image can also be reconstructed using the 1D samples as shown in Fig. 10. Mathematically, for every location $\mathbf{r}$ on the curve, we have that
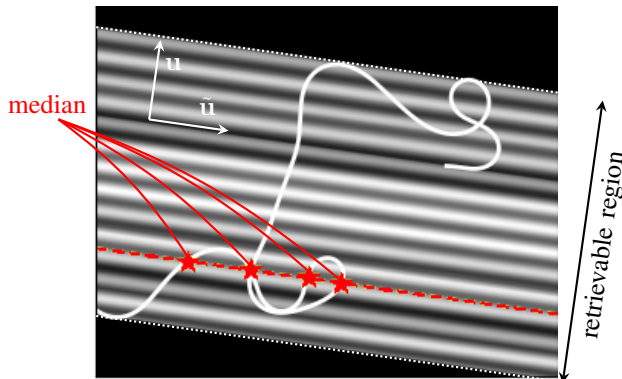

Fig. 10: Illustration of the image reconstruction scheme.

$$I(\mathbf{r} + \alpha\tilde{\mathbf{u}}) = I(\mathbf{r}), \ \alpha \in \mathbb{R}. \qquad (12)$$

This suggests a simple algorithm whereby, we reconstruct the pixel values of the image based on the their "backprojection" onto the trajectory (along the laminar direction $\tilde{\mathbf{u}}$). More precisely, if the backprojection intersects the curve at multiple points, we choose the median of the values at these points (more robustness to outliers). Moreover, this process provides a criterion for quantifying the quality of the trajectory retrieval: the 1D samples of the laminar image reconstructed using the above algorithm, along the trajectory retrieved in the previous subsection should match the 1D samples acquired by the mobile sensor. This matching accuracy is particularly useful in the practical cases where the ground-truth trajectory and image are unknown. A global view of the entire solution is shown in Fig. 9 and Algorithm. 1.

Algorithm 1: 2D Geometry Retrieval Algorithm

Input: 1D sample s_n, prior knowledge of curvature $\kappa_{\max}$
1: Determine segment length T (10)
2: **for** $l = 1$ to number of segments **do**
3:   Fit segment samples with a unique complex exponential (3)
4: **end for**
5: Track single frequency via the quadratic predictibility (See Sec. III-C)
6: Estimate generator frequency ω_g (8)
7: Calculate trajectory slopes based on its continuity (See Sec. III-D)
8: Reconstruct sampling trajectory (11)
9: Reconstruct image based on pixel backprojection onto the trajectory (12)

Output: Sampling trajectory and image.

IV. EXPERIMENTS

In this section, we demonstrate that the proposed algorithm is able to retrieve the 2D trajectory and the laminar image only from a sequence of 1D non-positioning samples of the image along that trajectory. We first validate the sampling theorem (i.e. Thm. 2) by simulations on synthetic laminar images in various conditions. Then, we demonstrate the robustness and accuracy of our algorithm by applying it to a number of real directional images. To perform these tests, we have implemented our algorithm in `python` on a MacBook Pro 2015 with a 4-core CPU and 16 GB of RAM. The whole computation time of each individual experiment is within 2 seconds.

A. Evaluation Metrics

In order to quantify the accuracy of our algorithm, we define two types of metrics:

1) *trajectory accuracy*: ideally, we would like to evaluate the smallest possible distance between the ground-truth curve, parametrized by $\mathbf{r}_0(t)$, and the reconstructed one, parametrized by $\mathbf{r}(t)$, up to a possible 2D perpendicular transformation $\mathbf{Q}$ (i.e., $\mathbf{Q}\mathbf{Q}^\mathsf{T} = \text{Identity}$) and a 2D

shift $\mathbf{q}$; more specifically, we would like to evaluate the absolute error (in pixels)

$$\inf_{\substack{\mathbf{q}\in\mathbb{R}^2 \\ \mathbf{Q}\,\text{perpendicular}}} \left(\int \frac{\inf_{t'}\|\mathbf{r}_0(t)-\mathbf{Q}\cdot\mathbf{r}(t')-\mathbf{q}\|^2\,\mathrm{d}t}{\text{length of curve}}\right)^{1/2}$$

However, for the sake of simplicity, we avoid performing the $\inf_{t'}$ by assuming that the two curves have the same parametrization, which leads to

$$\text{err}_{\text{trajectory}} \stackrel{\text{def}}{=} \inf_{\substack{\mathbf{q}\in\mathbb{R}^2 \\ \mathbf{Q}\,\text{perpendicular}}} \frac{\|\mathbf{r}_0(t)-\mathbf{Q}\mathbf{r}(t)-\mathbf{q}\|_2}{\sqrt{\text{length of curve}}} \quad \text{(in pixels)}$$

(13)

which is larger than the "ideal" error expression, but can be calculated exactly by solving an eigenvalue problem.

2) *image accuracy*: the matching accuracy between the samples $s(t) = I(\mathbf{r}(t))$ of the reconstructed image $I(\mathbf{r})$ along the reconstructed trajectory and the known samples $s_0(t)$ is quantified by the SNR

$$\text{err}_{\text{samples}} \stackrel{\text{def}}{=} 20\log_{10}\left(\frac{\|s_0(t)\|_2}{\|s(t)-s_0(t)\|_2}\right) \quad \text{(in dB)}$$

(14)

B. Tests with synthetic laminar images

We validate our theoretical results and the trajectory retrieval algorithm by conducting the following simulations. Varying parameters of the laminar image:

1) Dependence of the sinusoid fitting error on the dominant frequency;
2) Dependence of the sinusoid fitting error on the relative amplitude separation;

Varying parameters of the sampling trajectory:

1) Dependence of the curve reconstruction error on the trajectory curvature $\kappa_{\max}$;
2) Dependence of the curve reconstruction error on the trajectory length.

Robustness tests in the presence of noise are presented in the supplementary materials.

In all the experiments in this part, the univariate function g of the laminar image is made up of 20 sinusoids, an instance of which is shown in Fig. 1 (a) (1400×1400). The other quantities involved in Corollary 2 are left unchanged: $\Delta_0 = 0.7$, $T = 41$, $\Delta_1 = 1.2$.

Direction estimation — In this series of experiments, we vary the orientation of a single straight line along which we sample the laminar image, evaluate empirically the accuracy of the retrieved slope, which we compare to the prediction of Corollary 2. We manipulate one parameter of the laminar image at a time to assess its influence.

1) Main laminar frequency (ω_g)

Fig. 11 shows how the sinusoid-fitting error $\big||\hat{\omega}| - |\omega_g \mathbf{u}^\mathsf{T}\mathbf{a}|\big|$ changes with the scalar product $|\mathbf{u}^\mathsf{T}\mathbf{a}|$ (with $\|\mathbf{a}\|_2 = 1$) under two different values of ω_g. To better visualize the spread of this error, as well as its overall amplitude, 10 realizations (by randomly shifting the laminar image) are processed for each value of $|\mathbf{u}^\mathsf{T}\mathbf{a}|$. The corresponding image conditioning $\hat{\lambda}$ is:

1.312 ($\omega_g = 0.2$) and 6.888 ($\omega_g = 1.2$). The other quantities involved in Corollary 2 are left unchanged: $T = 41$, $\Delta_0 = 0.7$, $\Delta_1 = 1.2$ and $\gamma_0 = 0.5$.
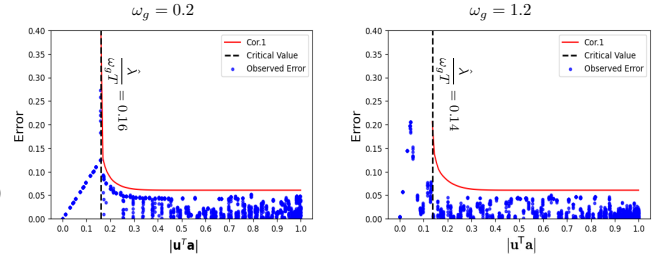

Fig. 11: Validation of Corollary 2: frequency estimation error in function of the slope of the line (i.e., $|\mathbf{u}^\mathsf{T}\mathbf{a}|$). Left: small laminar frequency ω_g (approximate $\hat{\lambda}/(\omega_g T)$ value is 0.12); right: large laminar frequency ω_g (approximate $\hat{\lambda}/(\omega_g T)$ value is 0.12).

As can be seen from Fig. 11, within the validity region specified by Corollary 2 (i.e., $|\mathbf{u}^\mathsf{T}\mathbf{a}| > \hat{\lambda}/(\omega_g T)$), the predicted value is effectively an upper bound of the estimation error, and this prediction is reasonably close to the actual (worse case) errors. We also see that the approximate value of $\hat{\lambda}/(\omega_g T)$ that we are proposing is reasonably close to the actual one.

2) Relative amplitude separation (γ_0)
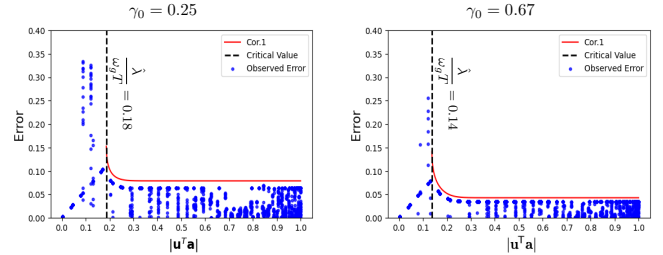

Fig. 12: Validation of Corollary 2: frequency estimation error in function of the slope of the line (i.e., $|\mathbf{u}^\mathsf{T}\mathbf{a}|$). Left: small relative amplitude difference γ_0 (approximate $\hat{\lambda}/(\omega_g T)$ value is 0.15); right: large relative amplitude difference γ_0 (approximate $\hat{\lambda}/(\omega_g T)$ value is 0.08).

Fig. 12 shows how the sinusoid-fitting error $\big||\hat{\omega}| - |\omega_g \mathbf{u}^\mathsf{T}\mathbf{a}|\big|$ changes with the scalar product $|\mathbf{u}^\mathsf{T}\mathbf{a}|$ (with $\|\mathbf{a}\|_2 = 1$) under two different values of γ_0, which controls how dominant the main laminar frequency ω_g is, relative to the others. To better visualize the spread of this error, as well as its overall amplitude, 10 realizations (by randomly shifting the laminar image) are processed for each value of $|\mathbf{u}^\mathsf{T}\mathbf{a}|$. The corresponding image conditioning $\hat{\lambda}$ is: 1.476 ($\gamma_0 = 0.25$) and 1.148 ($\gamma_0 = 0.67$). The other quantities involved in Corollary 2 are left unchanged: $\omega_g = 0.2$, $T = 41$, $\Delta_0 = 0.7$, and $\Delta_1 = 1.2$.

Again, within the validity region specified by Corollary 2 (i.e., $|\mathbf{u}^\mathsf{T}\mathbf{a}| > \hat{\lambda}/(\omega_g T)$), the predicted value is clearly an upper bound of the estimation error, and this prediction is reasonably close to the actual (worse case) errors. We also see

that the approximate value of $\hat{\lambda}/(\omega_g T)$ that we are proposing is reasonably close to the actual one.

Trajectory estimation — In this part, we investigate the accuracy of the trajectory estimation, depending on some of its characteristics (curvature, length). The laminar image, on the other hand, is kept unchanged from the previous experiments: $\omega_g = 0.2$, $T = 41$, $\Delta_0 = 0.7$, $\Delta_1 = 1.2$, and $\gamma_0 = 0.5$, which leads to $\hat{\lambda} = 0.902$.

Here, the sampling trajectory of the mobile sensor is parametrized by

$$\mathbf{r}_0(t) = \left(\int_0^T \cos\big(\theta(\tau)\big)\mathrm{d}\tau, \int_0^T \sin\big(\theta(\tau)\big)\mathrm{d}\tau\right)^{\mathsf{T}}.$$

where, by construction, $\theta'(t)$ is the curvature $\kappa(t)$ of the trajectory, given that t is its arclength. We express $\theta(t)$ as an M-periodic Fourier series

$$\theta(t) = \mathrm{Re}\left\{\sum_{k=0}^{K-1} \alpha_k \exp\left(j\frac{2\pi k t}{M}\right)\right\}$$

where α_k are generated randomly. This function changes all the more slowly as the curve length, M, is larger.

We use both the curve distance $\mathrm{err}_{\mathrm{trajectory}}$ and sample-mismatch level $\mathrm{err}_{\mathrm{samples}}$ to evaluate the trajectory reconstruction accuracy.
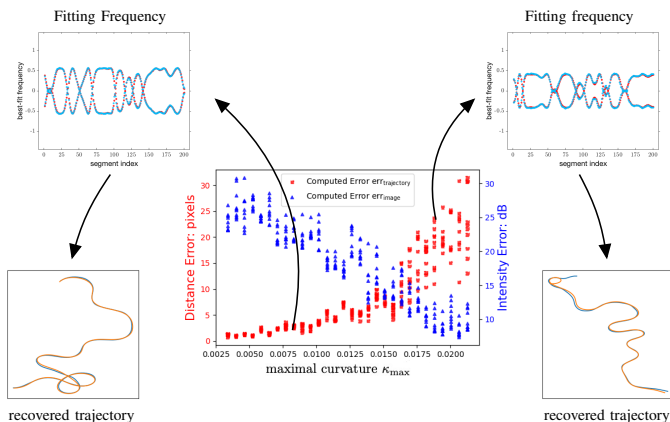
3) Effect of the curvature

recovered trajectory

Fig. 13: Center row: reconstruction error $\mathrm{err}_{\mathrm{trajectory}}$ and $\mathrm{err}_{\mathrm{samples}}$ vs κ_{max}, the maximal curvature of the trajectory. For each value of κ_{max}, ten realizations with random shifts of the trajectory are performed. Top row: ground-truth frequency (red), retrieved frequency (blue). Bottom row: ground-truth trajectory shown (red), reconstructed trajectory (blue).

By manipulating $\kappa_{\mathrm{max}} = \max_t |\theta'(t)|$, we can adjust the curvature of the sampling trajectory continuously. Fig. 13 shows how the two metrics that we have defined in (13) and (14) change, when the (maximal) curvature changes. As can be seen, in all cases the trajectory is recovered accurately (compared to the size of the image). In addition, the laminar image can also be reconstructed, and the resulting SNR varies from $8.42\,\mathrm{dB}$ (smallest curvature radius) to $31.24\,\mathrm{dB}$ (largest curvature radius). The relatively low SNR values may be

explained by an accumulation of inaccuracies on both the image and the trajectory.

Here, the range of "safe" curvature values (see Section III-B) is $\kappa \in [0.005, 0.009]$. Although smaller values also lead to high accuracy, it should be pointed out that for curvature smaller than 0.0025, we observe a loss of accuracy, as predicted in Hypothesis III-B.
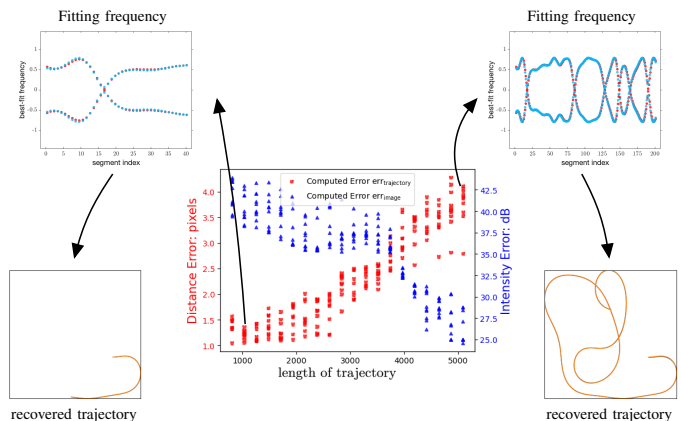
4) Effect of the length of the trajectory

recovered trajectory   recovered trajectory

Fig. 14: Center row: reconstruction error $\mathrm{err}_{\mathrm{trajectory}}$ and $\mathrm{err}_{\mathrm{samples}}$ vs trajectory length. For each curve length, ten realizations with random shifts of the trajectory are performed. Top row: ground-truth frequency (red), retrieved frequency (blue). Bottom row: ground-truth trajectory shown (red), reconstructed trajectory (blue).

Error accumulation is expected in our problem since what is estimated directly is essentially the derivative $\mathbf{r}'(t)$ of the trajectory. Intuitively, this drift is very likely to increase with the trajectory length, in line with our former results results [14, Theorem 2]). Yet, we observe that, in reality, the error accumulation rate is small.

Fig. 14 shows how the trajectory reconstruction error changes with the trajectory length. In all cases, the laminar image can be reconstructed accurately with a PSNR between $30\,\mathrm{dB}$ and $33\,\mathrm{dB}$. In all cases, it is impossible to visually distinguish between the ground-truth (red) and the retrieved trajectories (blue).

C. Tests with real images

In this subsection, we show that it is possible to retrieve trajectories sampled on real images that happen to be approximately laminar. To understand which real images are suitable for trajectory retrieval, we apply the following procedure

1) Using a rotation experiment with a segment length T that is as large as possible (e.g., the smallest dimension of the image), estimate the value of $\hat{\lambda}$ and ω_g (see Fig. 8), then check that, according to Hypothesis III-B, $\hat{\lambda} \leq 0.5\,\omega_g T$;
2) On the same rotation experiment, estimate γ_0 from the uncertainty of the best-fit frequency (7);
3) Choose T according to (10), which sets an upper limit of $1/(2T)$ to the maximal curvature κ_{max} (see Section III-B).

Larger values of T trade a lower trajectory slope uncertainty (hence, a higher accuracy of the trajectory itself) for a smaller curvature. In practice, when real images fail to be sufficiently laminar it is because the only trajectories that they allow to retrieve with acceptable accuracy, have a curvature that is so small that the value of T needed is larger than the size of the image.

ground-truth   reconstructed trajectory   frequency tracking
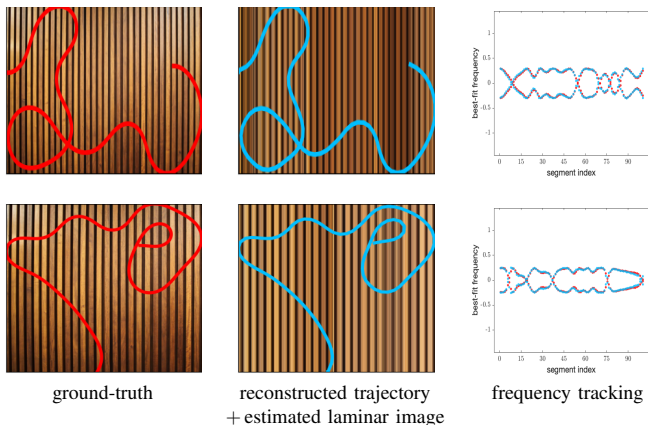+ estimated laminar image

Fig. 15: Reconstruction of trajectories from samples of two wood images, with maximum curvature $\kappa_{\max} = 0.009$ (top row) and $\kappa_{\max} = 0.018$ (bottom row). The reconstruction accuracy is: $\text{err}_{\text{trajectory}} = 8.65\,\text{pixels}$, $\text{err}_{\text{samples}} = 12.87\,\text{dB}$ (top); $\text{err}_{\text{trajectory}} = 10.46\,\text{pixels}$, $\text{err}_{\text{samples}} = 16.27\,\text{dB}$ (bottom). Image size: 768×1152.

There are important differences between the synthetic, perfectly laminar images that we have shown so far, and real, imperfectly laminar images:

- real images have a strong DC component (mean value) which means that the best-fit frequency is always zero. To mitigate this issue, we high-pass filter the 1D samples above an empirical low cutoff frequency value (typ. 0.01), hence preventing to estimate lower frequencies;
- real images frequently have too few pattern repetitions, making it impossible to improve accuracy by increasing the segment length T.

Typically, for imperfectly laminar real images, the link between best-fit frequency and the geometry $|\mathbf{u}^{\mathsf{T}}\mathbf{a}|$ is still valid locally, but the multiplication factor, ω_g, may vary (albeit slowly) along the samples, making it difficult to retrieve a complete trajectory with high accuracy without this information.

We first apply our algorithm to real wood textured images. As shown in Fig 15, trajectories with small curvature can be nicely retrieved with a good accuracy, demonstrating the feasibility of inferring geometry from one-dimensional samples. We use $T = 28$ so that the "safe" maximum trajectory curvature is $\kappa_{\max} = 0.018$. We also obtain $\omega_g = 0.243, \gamma_0 = 0.37$ and $\hat{\lambda} = 1.44 < 0.5\,\omega_g T = 3.4$ through the rotation pattern as described in Sec. II-C. As expected, a trajectory with smaller curvature $\kappa_{\max} = 0.009$ in Fig. 15 (top row), leads to a smaller reconstruction error than a larger curvature $\kappa_{\max} = 0.015$ (bottom row).

ground-truth   reconstructed trajectory   frequency tracking
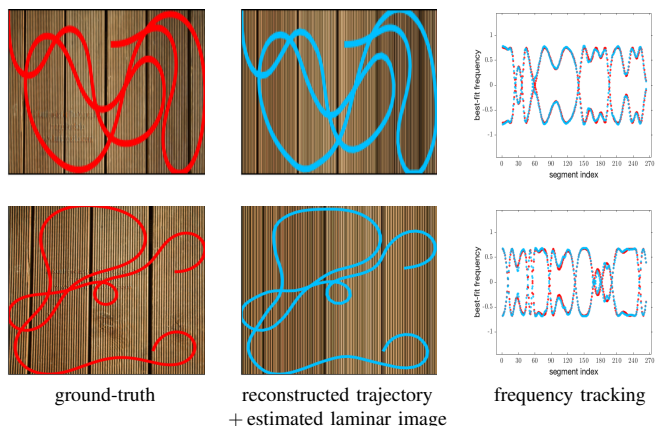+ estimated laminar image

Fig. 16: Reconstruction of trajectories from samples of two parts of wood boarding, with maximum curvature $\kappa_{\max} = 0.013$ (top row) and $\kappa_{\max} = 0.026$ (bottom row). The reconstruction accuracy is: $\text{err}_{\text{trajectory}} = 9.49\,\text{pixels}$, $\text{err}_{\text{samples}} = 11.05\,\text{dB}$ (top); $\text{err}_{\text{trajectory}} = 12.79\,\text{pixels}$, $\text{err}_{\text{samples}} = 12.00\,\text{dB}$ (bottom). Image size: 683×1024.

Real directional images with denser repetitions (i.e. larger ω_g) give rise to trajectory retrievals of more complex geometry (i.e., larger $\kappa_{\max}$), as seen in Fig. 16. Here, we use less samples ($T = 18$) in each trajectory segment, allowing a larger curvature $\kappa_{\max} = 0.028$. From a rotation experiment, we find $\omega_g = 0.612, \gamma_0 = 0.06$ and $\hat{\lambda} = 3.23 < 0.5\,\omega_g T = 5.51$. As expected, a trajectory with smaller curvature $\kappa_{\max} = 0.013$ (top row), leads to a smaller reconstruction error than a larger curvature $\kappa_{\max} = 0.026$ (bottom row), which is slightly above the "safe" curvature limit.

ground-truth   reconstructed trajectory   frequency tracking
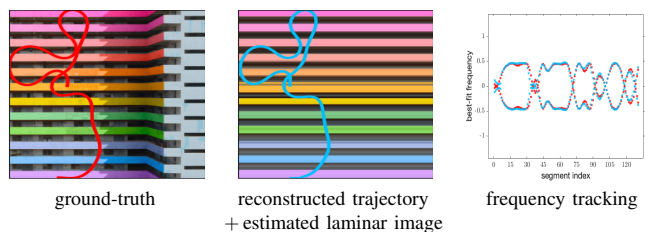+ estimated laminar image

Fig. 17: Reconstruction of a trajectory from samples of a rainbow building, with maximum curvature $\kappa_{\max} = 0.008$. The reconstruction accuracy is: $\text{err}_{\text{trajectory}} = 17.37\,\text{pixels}$, $\text{err}_{\text{samples}} = 12.90\,\text{dB}$. Image size: 2688×2160.

For less laminar images as shown in Figs. 17, and 18, a smaller ω_g implies a smaller curvature for a given segment length. In Fig. 17 where $T = 25$, the "safe" maximum trajectory curvature is 0.02, larger than the one shown here ($\kappa_{\max} = 0.008$). From a rotation experiment, we find $\omega_g = 0.368, \gamma_0 = 0.15$ and $\hat{\lambda} = 4.30 < 0.5\,\omega_g T = 4.60$. In Fig. 18 where $T = 20$, the "safe" maximum trajectory curvature is 0.025, larger than the one shown here ($\kappa_{\max} = 0.009$). From a rotation experiment, we find $\omega_g = 0.502, \gamma_0 = 0.10$ and $\hat{\lambda} = 4.73 < 0.5\,\omega_g T = 5.02$. It can be seen that the trajectories can all be accurately retrieved despite the fact that these images are not truly laminar.

Finally, we apply the algorithm to a grass image which is only approximately laminar (see Fig. 19)—a more challenging example. We sample this image along the same trajectory at two different locations: the first one (red curve) significantly more directional than the second one (blue curve). The difference in the accuracy of the frequency estimation leads to an obvious failure in the least directional case.

Notice that the laminar approximation of the image is less accurate compared to the trajectory reconstruction. This is mainly because these real images are not strictly laminar: there are actual pixel variations along the laminar direction in Figs. 15, 16, 17, and 18, although the hidden directionality contained within the 1D samples still makes it possible to retrieve the geometry of both the image and trajectory.

ground-truth   reconstructed trajectory   frequency tracking
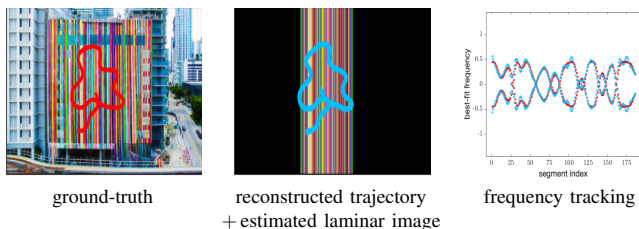   + estimated laminar image

Fig. 18: Reconstruction of a trajectory from samples of another rainbow building, with maximum curvature $\kappa_{max} = 0.009$. The reconstruction accuracy is: $\text{err}_{\text{trajectory}} = 8.47\,\text{pixels}$, $\text{err}_{\text{samples}} = 9.14\,\text{dB}$. Image size: 2850×2960.

Local Rotation Test   Local Rotation Test

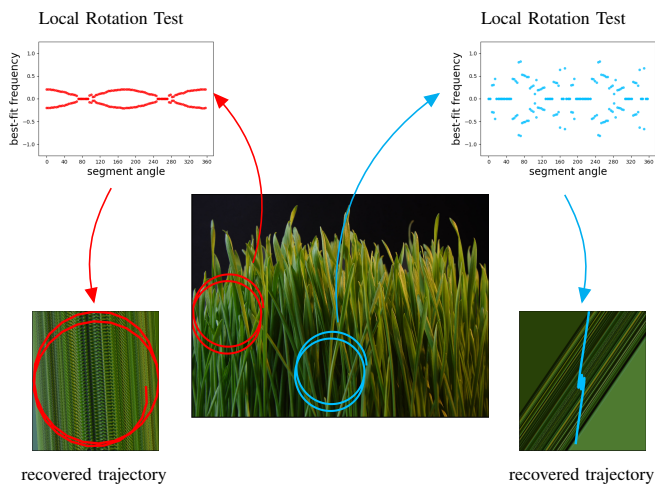recovered trajectory   recovered trajectory

Fig. 19: Reconstruction of the same trajectory at two locations in a grass image. In contrast to the reasonably accurate curve reconstruction on the left, a less directional image patch (right) results in a less reliable frequency estimation as exemplified by a local rotation test, hence a failed trajectory reconstruction.

V. Discussion and Future Work

The goal of this paper was to demonstrate that the geometry of the sampling scheme is, at least partially, embedded within

[0]The figure in Fig. 17 is selected from the photo gallery of photographer chakmkit: https://www.instagram.com/_chakmkit/; The building in Fig. 18 is the SLS Brickell Hotel & Residences in Miami (selected on Google Image: https://www.google.com/imghp?hl=en)

the 1D samples of an image that has some directionality. Simplifying our earlier approach [14], we have shown how to access this geometric information by fitting the samples locally with a single sinusoid, whose frequency is identified as the "slope" of the sampling trajectory. The visualization of this identification is made easy by rotation experiments that demonstrate this rotational continuity, when the image is sufficiently directional.

Unfortunately, using digital images with a fixed resolution inherently limits the reach of our demonstration. Yet, we want to outline that, in real-world applications, a mobile sensor moves and samples the analog field directly: no interpolation of gridded data is needed and so, no (grid-dependent) interpolation error is corrupting the samples, despite the very high 2D equivalent sampling resolution. Hence, our next focus will be to design a mobile sensing experiment and demontrate that the geometry of the trajectory can be inferred from the 1D samples acquired.

Although the accuracy of the reconstructed trajectories is good, the sample matching metrics indicates that, even in controlled (synthetic) cases, the laminar image approximation is not very accurate. This clearly calls for a higher quality algorithm than the simple approach proposed in Section III-E, which would also provide an accurate way to check the "laminarity" of the 1D samples.

It may seem that the laminar image hypothesis is very restrictive. However, it is possible to relax it by fitting the samples with more than one sinusoid (see [14]), or by looking for several local maxima of the single sinusoid fitting algorithm. These approaches can be made more robust by acquiring samples from more than one sensor, attached to the same mobile device.

One of our most speculative goals, is to apply this new type of 1D to 2D reconstruction as a visualization tool for non-geometric 1D signals like speech, music, EEG, seismograms etc. Although these signals are not known to be obtained from the samples of an image, making as if they were provides a new geometric representation, in which geometric clues could be exploited in applications like classification or recognition.

Appendix

A. Windowed sinusoidal fitting

Consider a signal $s(t)$ that can be expressed as $s(t) = \text{Re}\{c_0 e^{j\omega_0 t}\} + s_1(t)$ where $s_1(t) = \sum_{k=1}^{K} c_k e^{j\omega_k t}$, $c_0 \in \mathbb{C}$ and $\omega_0 > 0$. Given a window $w_T(t)$ which we choose according to (4), minimizing the fitting criterion

$$J(\omega) = \inf_{A \in \mathbb{C}} \int w_T(t) |s(t) - A e^{j\omega t}|^2 dt$$

over $\omega \in \mathbb{R}$ is equivalent to maximizing $|A_s(\omega)|$, where

$$A_s(\omega) = \int w_T(t) s(t) e^{-j\omega t} dt.$$

Lemma 1. *Assume that we have found two constants C and ε that satisfy the inequalities*

$$C \geq \sup_{\omega \in \mathbb{R}} |A_{s_1}(\omega)| \quad \text{and} \quad \varepsilon \geq |A_{s_1}(\pm\omega_0)|,$$

from which we define

$$Q = \frac{C + \varepsilon}{|c_0|} + 2\mathrm{e}^{-T^2\omega_0^2}.$$

If $Q < 1$, then the minimization of $J(\omega)$ over $\omega \in \mathbb{R}$ results in a frequency $\hat{\omega}$ which is such that

$$\big||\hat{\omega}| - |\omega_0|\big| \leq \underbrace{\frac{\sqrt{-\log(1 - Q)}}{T}}_{=\delta\omega}.$$

Proof. Without loss of generality, assume that $\omega_0 \geq 0$. The choice of $w_T(t)$ is equivalent to $\hat{w}_T(\omega) = \mathrm{e}^{-T^2\omega^2}$, which leads to

$$A_s(\omega) = c_0\hat{w}_T(\omega - \omega_0) + c_0^*\hat{w}_T(\omega + \omega_0) + A_{s_1}(\omega).$$

Obviously, we have that $|A_s(\pm\omega_0)| \leq |A_s(\hat{\omega})|$. Hence, given a positive number h, if we can prove that, for all ω that satisfy $\big||\omega| - \omega_0\big| > h$ we have $|A_s(\omega)| < |A_s(\pm\omega_0)|$, then this also proves that $\big||\hat{\omega}| - \omega_0\big| \leq h$. To this end, we need the following inequalities that are valid for all ω such that $\big||\omega| - \omega_0\big| > h$

- Lower bound of the maximum:
$$\begin{aligned}|A_s(\pm\omega_0)| &\geq |c_0\hat{w}_T(0) + c_0^*\hat{w}_T(2\omega_0)| - |A_{s_1}(\pm\omega_0)|\\ &\geq |c_0|\big(\hat{w}_T(0) - \hat{w}_T(2\omega_0)\big) - \varepsilon\\ &\geq |c_0|\big(1 - \hat{w}_T(\omega_0)\big) - \varepsilon\end{aligned}$$

- Upper bound of the non-maximum:
$$\begin{aligned}|A_s(\omega)| &\leq |c_0|\big(\hat{w}_T(\omega - \omega_0) + \hat{w}_T(\omega + \omega_0)\big) + |A_{s_1}(\omega)|\\ &\leq |c_0|\big(\hat{w}_T(|\omega| - \omega_0) + \hat{w}_T(|\omega| + \omega_0)\big) + C\\ &\leq |c_0|\big(\hat{w}_T(\big||\omega| - \omega_0\big|) + \hat{w}_T(\omega_0)\big) + C\\ &< |c_0|\big(\hat{w}_T(h) + \hat{w}_T(\omega_0)\big) + C\end{aligned}$$

Both inequalities are proven using the triangular inequality and the monotonous decrease of $\hat{w}_T(\omega)$ when $\omega \geq 0$. We can thus state that, if h is chosen such that

$$|c_0|\big(\hat{w}_T(h) + \hat{w}_T(\omega_0)\big) + C = |c_0|\big(1 - \hat{w}_T(\omega_0)\big) - \varepsilon$$

then, for all ω such that $\big||\omega| - \omega_0\big| > h$, we have $|A_s(\omega)| < |A_s(\pm\omega_0)|$. As argued previously, this ensures that $\big||\hat{\omega}| - \omega_0\big| \leq h$, a result that it is straightforward to generalize to $\omega_0 < 0$. Of course, the value of h that satisfies this equation is identical to $\delta\omega$, given the expression of $\hat{w}_T(\omega)$. $\qquad\square$

B. Upper bound of a sum of Gaussians

Lemma 2. *We are given an increasing real sequence x_k, $k \in \mathbb{Z}$. Denoting by $\Delta = \inf_k |x_{k+1} - x_k|$ their minimal separation, we have*

$$\sum_{k \in \mathbb{Z}} \mathrm{e}^{-(x - x_k)^2} \leq 1 + \frac{\mathrm{e}^{-\Delta^2/4}}{1 - \mathrm{e}^{-3\Delta^2/4}}, \qquad (15)$$

for all $x \in \mathbb{R}$.

Proof. Denote by $f(x)$ the function on the lhs of (15). Assume that its maximum is attained at $x \in [x_0, (x_0 + x_1)/2]$ then

- when $k \geq 1$, we find that $x_k - x \geq \Delta/2 + (k-1)\Delta$ and so, $\exp\big(-(x - x_k)^2\big) \leq \exp\big(-(k - 1/2)^2\Delta^2\big)$;
- when $k \leq -1$, we find that $x - x_k \geq |k|\Delta$ and so, $\exp\big(-(x - x_k)^2\big) \leq \exp\big(-k^2\Delta^2\big)$.

Hence, if the maximum of $f(x)$ is attained at $x \in [x_0, (x_0 + x_1)/2]$ we can bound this maximum by

$$f(x) \leq 1 + \sum_{k \leq -1} \mathrm{e}^{-k^2\Delta^2} + \sum_{k \geq 1} \mathrm{e}^{-(k-1/2)^2\Delta^2} = \sum_{k \geq 0} \mathrm{e}^{-k^2\Delta^2/4}.$$

For symmetry reasons (consider $f(-x)$), this bound is also valid if the maximum of $f(x)$ is attained at $x \in [(x_0 + x_{-1})/2, x_0]$ instead. Of course, we would also find the same bound if the maximum of $f(x)$ were attained in the interval $[(x_k + x_{k-1})/2, (x_k + x_{k+1})/2]$, which shows its generality.

Using the inequality $k^2 \geq 3k - 2$ for $k \geq 1$ allows to simplify this infinite summation:

$$\begin{aligned}\sum_{k \geq 0} \mathrm{e}^{-k^2\Delta^2/4} &\leq 1 + \sum_{k \geq 1} \mathrm{e}^{-(3k-2)\Delta^2/4}\\ &\leq 1 + \mathrm{e}^{-\Delta^2/4}\sum_{k \geq 0} \mathrm{e}^{-3k\Delta^2/4}\\ &\leq 1 + \frac{\mathrm{e}^{-\Delta^2/4}}{1 - \mathrm{e}^{-3\Delta^2/4}}.\end{aligned}$$

$\qquad\square$

C. Proof of Theorem 2

Proof. Along the straight line defined by $\mathbf{r}(t) = t\mathbf{a} + \mathbf{b}$, the samples $s(t) = I\big(\mathbf{r}(t)\big)$ take the form

$$\begin{aligned}s(t) = &\underbrace{\mathrm{Re}\big\{c_0\exp(j\boldsymbol{\omega}_0^\mathsf{T}\mathbf{b})\exp(j\boldsymbol{\omega}_0^\mathsf{T}\mathbf{a}t)\big\}}_{\mathrm{Re}\{c_0'\mathrm{e}^{j\omega_0 t}\}}\\ &+ \sum_{k=1}^K c_k\underbrace{\exp(j\boldsymbol{\omega}_k^\mathsf{T}\mathbf{b})\exp(j\boldsymbol{\omega}_k^\mathsf{T}\mathbf{a}t)}_{c_k'\mathrm{e}^{j\omega_k t}}.\end{aligned}$$
$$\underbrace{\phantom{+ \sum_{k=1}^K c_k\exp(j\boldsymbol{\omega}_k^\mathsf{T}\mathbf{b})\exp(j\boldsymbol{\omega}_k^\mathsf{T}\mathbf{a}t)}}_{=s_1(t)}$$

The proof is then a direct application of Lemma 1, for which we have to find the bounds C and ε. Given the expression of $s_1(t)$ as a sum of complex exponentials, we have to majorize

$$\begin{aligned}\left|\sum_{k=1}^{+\infty} c_k'\mathrm{e}^{-T^2(\omega - \omega_k)^2}\right| &\leq \sup_{k \geq 1}|c_k'|\sum_{k=1}^{+\infty} \mathrm{e}^{-T^2(\omega - \omega_k)^2}\\ &\leq \sup_{k \geq 1}|c_k'|\left(1 + \frac{\mathrm{e}^{-T^2\Delta_1^2/4}}{1 - \mathrm{e}^{-3T^2\Delta_1^2/4}}\right)\\ &= C \quad \text{(Lemma 2)}\end{aligned}$$

and

$$\begin{aligned}\left|\sum_{k=1}^{+\infty} c_k'\mathrm{e}^{-T^2(\pm\omega_0 - \omega_k)^2}\right| &\leq \sup_{k \geq 1}|c_k'|\sum_{k=1}^{+\infty} \mathrm{e}^{-T^2(\pm\omega_0 - \omega_k)^2}\\ &\leq \sup_{k \geq 1}|c_k'|\sum_{k=1}^{+\infty} 2\mathrm{e}^{-k^2T^2\Delta_0^2}\\ &\leq \sup_{k \geq 1}|c_k'|\frac{2\mathrm{e}^{-T^2\Delta_0^2}}{1 - \mathrm{e}^{-3T^2\Delta_0^2}} = \varepsilon\end{aligned}$$

where $\Delta_0 = \inf_{k \geq 1}\big(|\omega_k - \omega_0|, |\omega_k + \omega_0|\big)$ and $\Delta_1 = \inf_{k \neq k' \geq 1}|\omega_k - \omega_{k'}|$. Given that $\sup_{k \geq 1}|c_k'| = \sup_{k \geq 1}|c_k|$, the statement of the Theorem follows from Lemma 1. $\qquad\square$

D. Proof of Corollary 2

Proof. This is a direct application of Theorem 2, because we have $\inf_{k\geq 1}\left(|(\boldsymbol{\omega}_k-\boldsymbol{\omega}_0)^\mathsf{T}\mathbf{a}|, |(\boldsymbol{\omega}_k+\boldsymbol{\omega}_0)^\mathsf{T}\mathbf{a}|\right) = \Delta_0\omega_g|\mathbf{u}^\mathsf{T}\mathbf{a}|$ and $\inf_{k\neq k'\geq 1}|(\boldsymbol{\omega}_k-\boldsymbol{\omega}_{k'})^\mathsf{T}\mathbf{a}| = \Delta_1\omega_g|\mathbf{u}^\mathsf{T}\mathbf{a}|$. Then, the factor Q involved in Theorem 2 is identical to $Q(\omega_g T\mathbf{u}^\mathsf{T}\mathbf{a})$ here.

We need to find for which values of $\lambda \geq 0$ we have $Q(\lambda) < 1$. We notice that $Q(\lambda)$ is continuous and decreases monotonously from $+\infty$ to $1 - \gamma_0$ when λ increases from 0 to $+\infty$. Given that, by hypothesis, $1 - \gamma_0 < 1$, there exists a unique value $\hat{\lambda} > 0$ for which $Q(\hat{\lambda}) = 1$.

A lower bound on $\hat{\lambda}$ can be found by analyzing the dominant terms in the expression $Q(\lambda)$:

1) $(1-\gamma_0) + 2\mathrm{e}^{-\hat{\lambda}^2} < 1$, which directly leads to $\hat{\lambda} > \sqrt{-\log\gamma_0}$.

2) $(1-\gamma_0)(1 + \frac{\mathrm{e}^{-\Delta_1^2\hat{\lambda}^2/4}}{1-\mathrm{e}^{-3\Delta_1^2\hat{\lambda}^2/4}}) < 1$, which shows that $\mathrm{e}^{-\Delta_1^2\hat{\lambda}^2/4} < \gamma_1$, if we denote by γ_1 the unique real solution of the cubic equation

$$\gamma_1^3 + \frac{1-\gamma_0}{\gamma_0}\gamma_1 - 1 = 0.$$

Equivalently, we have $\hat{\lambda} > 2\Delta_1^{-1}\sqrt{-\log\gamma_1}$ where the root γ_1 is found using Cardano-Tartaglia's formula [18].

3) $(1-\gamma_0)(1 + \frac{2\mathrm{e}^{-\Delta_0^2\hat{\lambda}^2}}{1-\mathrm{e}^{-3\Delta_0^2\hat{\lambda}^2}}) < 1$, which shows that $\mathrm{e}^{-\Delta_0^2\hat{\lambda}^2} < \gamma_2$, if we denote by γ_2 the unique real solution of the cubic equation

$$\gamma_2^3 + \frac{2(1-\gamma_0)}{\gamma_0}\gamma_2 - 1 = 0.$$

Equivalently, we have $\hat{\lambda} > \Delta_0^{-1}\sqrt{-\log\gamma_2}$ where the root γ_2 is found using Cardano-Tartaglia's formula.

Hence, we find that $\hat{\lambda}$ is lower bounded by the maximum of these three values, as stated in the Corollary Empirically, this bound is close to the true value when one of the three terms (typically, the one derived from γ_1) is dominant. $\square$

REFERENCES

[1] HyungJune Lee, Martin Wicke, Branislav Kusy, and Leonidas Guibas. Localization of mobile users using trajectory matching. In *Proceedings of the first ACM international workshop on Mobile entity localization and tracking in GPS-less environments*, pages 123–128, 2008.

[2] Ayoung Kim and Ryan M Eustice. Perception-driven navigation: Active visual slam for robotic area coverage. In *2013 IEEE International Conference on Robotics and Automation*, pages 3196–3203. IEEE, 2013.

[3] S. Ehsan, K. Bradford, M. Brugger, B. Hamdaoui, Y. Kovchegov, D. Johnson, and M. Louhaichi. Design and analysis of delay-tolerant sensor networks for monitoring and tracking free-roaming animals. *IEEE Transactions on Wireless Communications*, 11(3):1220–1227, March 2012.

[4] M. L. Yin and R. Arellano. A risk analysis framework on GPS user range accuracy. In *2012 Proceedings Annual Reliability and Maintainability Symposium*, pages 1–6, Jan 2012.

[5] Xinwei Wang, Ole Bischoff, Rainer Laur, and Steffen Paul. Localization in wireless ad-hoc sensor networks using multilateration with rssi for logistic applications. *Procedia Chemistry*, 1(1):461–464, 2009.

[6] H. P. Tan, Z. A. Eu, and W. K. G. Seah. An enhanced underwater positioning system to support deepwater installations. In *OCEANS 2009*, pages 1–8, Oct 2009.

[7] Neal Patwari, Alfred O Hero, Matt Perkins, Neiyer S Correal, and Robert J O'dea. Relative location estimation in wireless sensor networks. *IEEE Transactions on signal processing*, 51(8):2137–2148, 2003.

[8] Nissanka Bodhi Priyantha, Hari Balakrishnan, Erik D Demaine, and Seth Teller. Mobile-assisted localization in wireless sensor networks. In *Proceedings IEEE 24th Annual Joint Conference of the IEEE Computer and Communications Societies.*, volume 1, pages 172–183. IEEE, 2005.

[9] Konrad Lorincz and Matt Welsh. Motetrack: A robust, decentralized approach to rf-based location tracking. In *International Symposium on Location-and Context-Awareness*, pages 63–82. Springer, 2005.

[10] Arvind Thiagarajan, Lenin Ravindranath, Hari Balakrishnan, Samuel Madden, and Lewis Girod. Accurate, low-energy trajectory mapping for mobile devices. 2011.

[11] Chi Hay Tong, Timothy D Barfoot, and Érick Dupuis. Three-dimensional slam for mapping planetary work site environments. *Journal of Field Robotics*, 29(3):381–412, 2012.

[12] Denis Chekhlov, Andrew P Gee, Andrew Calway, and Walterio Mayol-Cuevas. Ninja on a plane: Automatic discovery of physical planes for augmented reality using visual slam. In *2007 6th IEEE and ACM International Symposium on Mixed and Augmented Reality*, pages 153–156. IEEE, 2007.

[13] R. Guo and T. Blu. FRI sensing: Sampling images along unknown curves. In *ICASSP 2019 - 2019 IEEE International Conference on Acoustics, Speech and Signal Processing (ICASSP)*, pages 5132–5136, May 2019.

[14] R. Guo and T. Blu. FRI sensing: Retrieving the trajectory of a mobile sensor from its temporal samples. *IEEE Transactions on Signal Processing*, 68:5533–5545, 2020.

[15] C. Gilliam and T. Blu. Fitting instead of annihilation: Improved recovery of noisy FRI signals. In *2014 IEEE International Conference on Acoustics, Speech and Signal Processing (ICASSP)*, pages 51–55, May 2014.

[16] Daniel Rouseff. Effect of shallow water internal waves on ocean acoustic striation patterns. *Waves in Random Media*, 11(4):377–394, 2001.

[17] R. Guo and T. Blu. FRI sensing: 2D localization from 1D mobile sensor data. In *2020 Asia-Pacific Signal and Information Processing Association Annual Summit and Conference (APSIPA ASC)*, pages 986–991, 2020.

[18] Lucye Guilbeau. The history of the solution of the cubic equation. *Mathematics News Letter*, pages 8–12, 1930.